Was the January 26th, 1700 Cascadia Earthquake Part of an Event Sequence?

Diego Melgar[1*]

[1]Department of Earth Sciences, University of Oregon, Eugene, OR

[*] dmelgarm@uoregon.edu

Was the January 26th, 1700 Cascadia Earthquake Part of an Event Sequence?

Diego Melgar[1*]

[1]Department of Earth Sciences, University of Oregon, Eugene, OR

[*] dmelgarm@uoregon.edu

Key Points

- We simulate 32,500 1700 Cacadia earthquake ruptures in the range M7.8-M9.6 and model the tsunamis
- We test which models match coastal subsidence estimates and the historical tsunami in Japan
- We find that the data can be explained by sequences of as many as five earthquakes

Abstract

Coastal subsidence, dating of soil samples and tree rings, and sedimentological evidence of a tsunami point to coseismic activity on a sizable portion of the Cascadia subduction zone circa 1700. Documents from Japan reveal that on January 26th of that year there were tsunami impacts across distant locations in the country and past modeling shows that a large Cascadia earthquake is the most likely source. The prevailing hypothesis is that only a single large event rupturing the entire plate boundary can explain these observations. Here we model tens of thousands of ruptures and simulate their coastal subsidence and far-field tsunami signals and show that it is possible that the 1700 earthquake was instead part of a sequence of several earthquakes. Partial rupture of as little as ~40% of the along-strike extent of the megathrust in one large M>8.7 earthquake can explain the tsunami in Japan and a part of the coastal subsidence. As many as four more earthquakes with M<8.6 can complete the coseismic subsidence signal without their tsunamis being large enough to be recorded in Japan. Given the spatial gaps in the presently available geologic estimates of coastal subsidence data it is also possible that short segments of the megathrust have remained unbroken. The findings have significant implications for Cascadia geodynamics and how earthquake and tsunami hazards in the region are quantified.

1. Motivation and Background

There is significant evidence that a great earthquake took place on the Cascadia subduction zone (CSZ, Figure 1A) on January 26th, 1700 (Atwater et al., 2005; Walton et al., 2021). From northern California to Vancouver Island there is widespread occurrence of sequences of tidal wetland soil overlain by mud as a result of coseismic subsidence (Atwater et al., 1987; Nelson et al., 1996; Witter et al., 2003)(Figure 1B). Additionally, there are margin-wide abrupt contacts of sand over the mud deposits which represent deposition by a tsunami following the sudden subsidence (Atwater el al, 1995). Radiocarbon dating at many of these sites can only narrow the timing of subsidence at ~100-400 years before present (BP) (Shennan et al., 1996). Meanwhile, at particularly well-preserved locations in southern Washington and Northern California, high-precision dating of tree rings as well as of rhizomes brackets the potential interval of deformation to the years ~1690-1720 (Atwater & Yamaguchi, 1991, Nelson et al., 1995). Similarly, offshore observations of turbidites correlate well across the margin and suggest episodes of strong shaking across most if not the full extent of the subduction zone with the latest occurring 260+/-120 Yrs BP (Goldfinger et al., 2012).

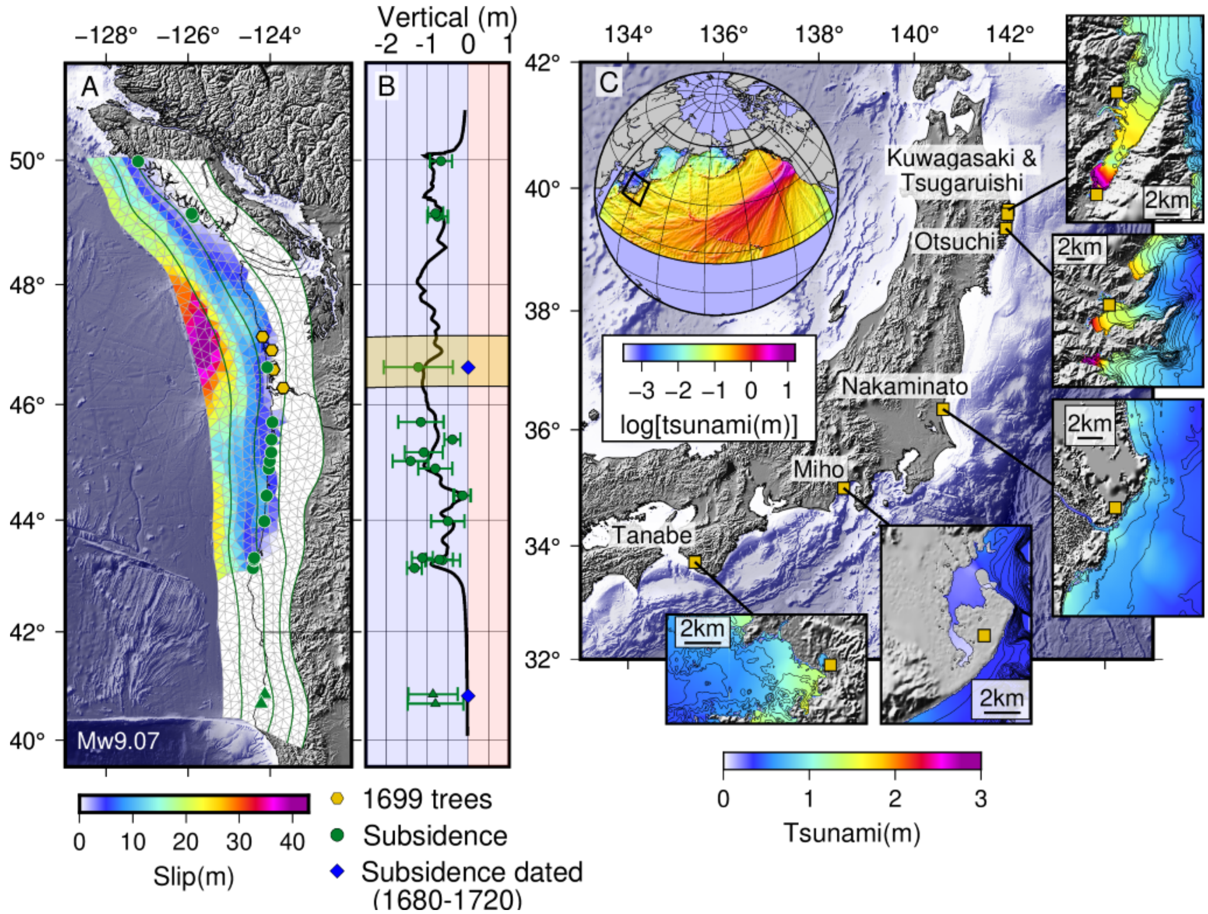

Figure 1. *(A) The Cascadia subduction zone. Shown is an example synthetic slip model. The 3D megathrust geometry (Hayes et al., 2018) is shown with depth contours at 10km intervals. Green symbols are the locations of coseismic coastal subsidence estimates. Yellow hexagons are the locations of the 1699 western red cedar trees. (B) Paleogeodetic subsidence from a combination dataset (Leonard et al., 2010; Kemp et al., 2018). Symbols are the the estimates with error bars. The thick black line is the coastal subsidence from the coseismic slip model in (A). Shaded region is the location of the 1699 trees and blue diamonds locations where subsidence is dated with high-resolution. (C) Tsunami produced by the slip model in (A). The inset shows the open ocean amplitudes across the Pacific Ocean in the modeled domain. Shown as well are the amplitudes at five locations in Japan where estimates of tsunami inundation are available from historical documents (Satake et al., 2003). Black lines are the contours of the high-resolution bathymetry at 10m intervals.*

While compelling, these data do not narrow down the timing of the last great earthquake to a specific year or day. This constrain is from two other key observations. The first is of seven western red cedar trees along an ~100km stretch of Southern Washington (Figure 1A) which clearly show that they last generated bark sometime in the year 1699 and before the spring of 1700 before being killed by rapid submergence into intertidal waters (Yamaguchi et al., 1997). Precise dating of these "1699 trees" was possible by correlation of the ring patterns to nearby living "witness" trees and has not been carried out elsewhere in the subduction zone. The second observation arises from the discovery of written documents in Japan (Satake et al, 1996; 2003) that detail observations of a tsunami which caused widespread damage at locations as far as ~800km apart on the main island of Honshu (Figure 1C). Because the tsunami was not accompanied by any documented shaking, the event is often named the "orphan" tsunami and is inferred to have its origin elsewhere in the Pacific basin. Its timing does not correlate to any known large earthquake in Kamchatka, the Aleutians, or South America (Satake et al., 2003). The amplitudes of the inundation in Japan (Figure 1C,2) have been deduced from the written accounts and corrected for the tides and post-1700 land-level changes and hydrodynamic modeling has shown that an M8.7-M9.2 earthquake at the CSZ could satisfy them. Based on the tsunami travel times this places the origin of the earthquake somewhere on the 26th of January 1700.

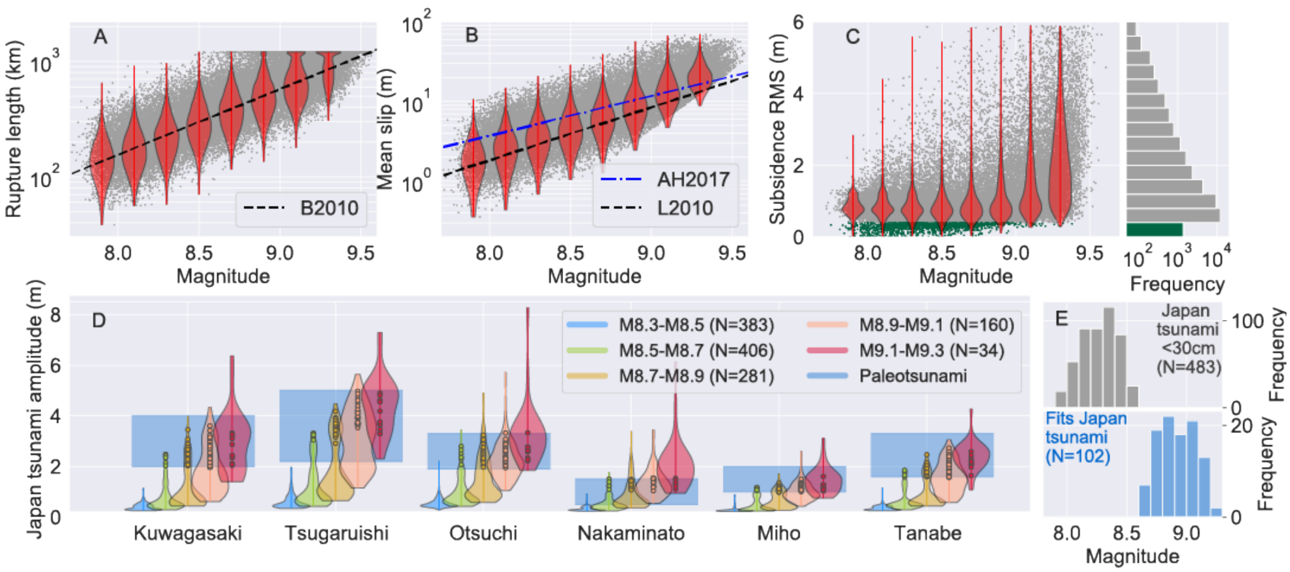

Figure 2. *(A) Rupture length as a function of magnitude for the 32,500 models. Grey dots are individual events. The red violins show estimates of the length distributions at 0.2 unit bins. The dashed line labeled B2010 are the mean lengths expected from a scaling law (16). (B) Same as (A) but showing mean slip as a function of magnitude. The lines labeled AH2017 and L2010 are the expected values from scaling laws (Allen & Hayes, 2017; Leonard , 2010). (C) RMS misfit between the predicted coastal subsidence and the paleogeodetic estimates in Fig 1B. The green dots are the 1,034 ruptures with RMS<0.4 used for tsunami modeling. (D) Tsunami modeling results for the 1,034 ruptures with RMS<0.4. Shown are the amplitudes at five locations in Japan (Figure 1C) as a function of magnitude. The violins show the distribution for all events, the dots show 102 ruptures which fit the observations at all sites. Shaded blue regions are the inferred amplitudes from historical records (Satake et al., 2003). (E) Histograms of the magnitude distribution of 102 events that fit the Japan tsunami data and 483 events that are considered to produce amplitudes that are too small (<30cm) to have been recorded on historical documents.*

Was the 1700 earthquake a single event or was it a sequence of progressive failures of the megathrust in more modestly sized (~M8) earthquakes over several decades? This is fundamental to understanding the long term seismogenic behavior of the CSZ and for quantifying future hazards potentials. A sequence of events can explain the paleogeodetic coastal subsidence (Nelson et al., 1995; McCaffrey & Goldfinger, 1995). However, the subsequent unearthing of the historical documents in Japan, and the inferred tsunami inundation amplitudes have been interpreted to rule this out. While coastal subsidence can be explained by numerous smaller events, tsunami modeling with quasi-homgenous slip sources was used to argue that ~M8 earthquakes produce amplitudes in Japan that are an order of magnitude too small (Satake et al., 2003). This, conjoined with the location of the precisely dated 1699 trees, roughly in the geographic middle of the subduction zone, has been interpreted as definitive evidence that only a single plate-boundary-wide large magnitude event could explain all data simultaneously (Atwater et al., 2005). To date this single-event model is the dominant view (Walton et al., 2021) and almost taken as axiomatic.

For earthquakes before 1700 there is abundant onshore evidence of smaller ~M8 ruptures, particularly in southern Oregon (Witter et al., 2003; Kelsey et al., 2002; Walton et al., 2021). This is supported by the turbidite record offshore (Goldfinger et al., 2012) as well. This has led to the perspective that, over many earthquake cycles, the plate boundary has more than one mode of failure. In addition to margin-scale events it can also rupture in sequences of smaller earthquakes spanning a few decades (Nelson et al., 2006). In this view, the two modes of failure are independent of each other and formal hazards assessments for the region conceptualize them as two distinct possibilities (Frankel et al., 2015) when considering future ruptures.

When the 1700 tsunami was first modeled, only four different fault dimensions were considered and only one-dimensional distributions of slip, symmetric along the strike of the fault, were used. However, over the last decade our perspective on large earthquake sources has sharpened. Routine inversion of geodetic and seismological data has allowed us to build databases of earthquake source parameters. From these, source scaling laws have been defined that describe empirical probability density functions of the expected areal extent of earthquakes of a certain magnitude (Blaser et al., 2010; Leonard et al., 2010, Allen & Hayes, 2017). Not all events of a given magnitude have equal rupture dimensions. For example, the 2010 M8.8 Maule earthquake ruptured for 500km, the 2011 M9.0 Tohoku-oki ruptured 400km, and the 2004 M9.2 Sumatra earthquake ruptured 1,400km.

Additionally, we now have models of the heterogenous slip distributions for most large earthquakes since 1990 (Ye et al., 2016; Hayes, 2017) and the variability in how slip is distributed over the faults is significant. For tsunami modeling this is important. The initial tsunami potential energy directly controls the inundation amplitudes and depends non-linearly on slip (Nosov et al., 2014). As a result, even if the rupture dimensions and magnitude are held fixed, the tsunami amplitudes produced by homogenous or near-homogeous slip distributions, such as those previously used to study the 1700 earthquake, and those produced by heterogenous slip distributions can vary substantially (Melgar et al., 2019). It has been found that systematically larger tsunamis result when considering heterogenous over homogenous slip.

This new perspective on the heterogeneities of large earthquakes has also led to advances in generating synthetic earthquake rupture models (LeVeque et al., 2016; Frankel et al., 2018). It is now commonplace for both seismic and tsunami source and hazards studies to generate “stochastic” ruptures. These are constrained by known quantities, such as the fault geometry, and an Earth structure model, but are allowed randomly to vary in area, and slip distribution based on assumed probability density functions for these parameters.

Given the progress in the observation of large earthquakes and in modeling ruptures and tsunamis it is pertinent to revisit the January 26th 1700 Cascadia earthquake. Here we will use these new advances and model 32,500 ruptures on the 3D slab geometry of the CSZ in the M7.8 - M9.6 range. We will also carry out hydrodynamic modeling of their resulting tsunamis with high-resolution bathymetry. Our findings will be used to argue that the coastal subsidence data and the far-field tsunami amplitudes in Japan can be explained with a mixed mode sequence of earthquakes. Such a sequence would be comprised of one large (M>8.7) earthquake, the mainshock, that ruptures only part of the plate boundary and is preceded or followed by one or many smaller events in the ~M8-M8.6 range. Our findings do not rule out the single event hypothesis and we will show examples of single-earthquake plate boundary spanning events that explain the observations. However, we find strong evidence, that the prevailing view, that the geological and far-field tsunami data definitively rule out partial rupture of the CSZ in 1700, is overly simplistic and cannot at present be justified. That the January 26th 1700 event is part of a longer-lived sequence of earthquakes, potentially spanning many decades, needs to be considered as a hypothesis that is at least equally likely.

2. Data and Methods

2.1 Rupture modeling

The process for generating the stochastic rupture models is described in great detail in Melgar et al., (2016), Goldberg & Melgar (2020) and Small & Melgar (2021). Here we summarize the most important aspects. We use the 3D megathrust for the CSZ from Slab2.0 (Figure 1A, Hayes et al., 2018) and discretize it into a triangular mesh using a finite element meshing software. We use the slab model only to a maximum depth of 40km. This is well into the slow slip region (Bartlow, 2020) but does not necessarily mean slip is allowed to extend to this depth, as will be discussed in a moment. Given an assumed magnitude, the length and width of the fault is determined by making a random draw from the lognormal distriubtions of Blaser et al. (2010). This ensure that not all events of similar magnitudes have the same fault dimensions. The stochastic slip distribution is generated using the well-known result that slip can be conceptualized as a spatially random field defined with a VonKarman auto-correlation function (VK-ACF, Mai & Beroza, 2002) and a slip standard deviation (Melgar & Hayes, 2019). The VK-ACF is completely defined by three critical parameters. The Hurst exponent and the along-strike and along-dip correlation lengths. These later two control the predominant size of the asperities in the resulting slip pattern while the Hurst exponent controls the amount of short wavelength structure in between the larger asperities. Scaling laws for the correlation lengths have been determined by measuring them from databases of slip models (Mai & Beroza, 2002; Melgar & Hayes, 2019) where it has been found that they correlate strongly to length and width of the causative earthquake. Here we use the scaling laws defined by Melgar & Hayes (2019) measured from the US Geological Survey's database of large earthquake slip models. The Hurst exponent meanwhile has a very weak or no correlation with magnitude, length, or width and is typically assumed constant. Here we use the value H = 0.4 also obtained from the analysis of Melgar & Hayes (2019).

Once all the parameters of the correlation matrix are defined, the stochastic slip pattern can be obtained. This is most commonly done in the wavenumber domain (e.g. Graves & Pitarka, 2010). However, here we do it directly in the spatial domain using the Karhunen-Loeve (KL) expansion approach proposed by LeVeque et al. (2016). The stochastic vector, *s*, containing the slip values at each subfaultt (the slip distribution) is obtained from

$$\bar{s} = \bar{\mu} + \sum_{k=1}^{N} z_k \lambda_k \bar{v}_k \quad . \tag{1}$$

$\bar{\mu}$, is the mean of $\bar{s}$ and the desired statistics are enforced by the eigenvalues, λ_k and eigenvectors, $\bar{v}_k$, of the assumed VonKarman ACF. z_k are normally distributed random numbers with a mean of 0 and a standard deviation of 1 which introduce the desired stochastic variability. N is the number of eigenmodes which corresponds to the number of subfaults or elements of s. Figures 1A,3 and Figures S1-S4 are example of ruptures generated with this approach.

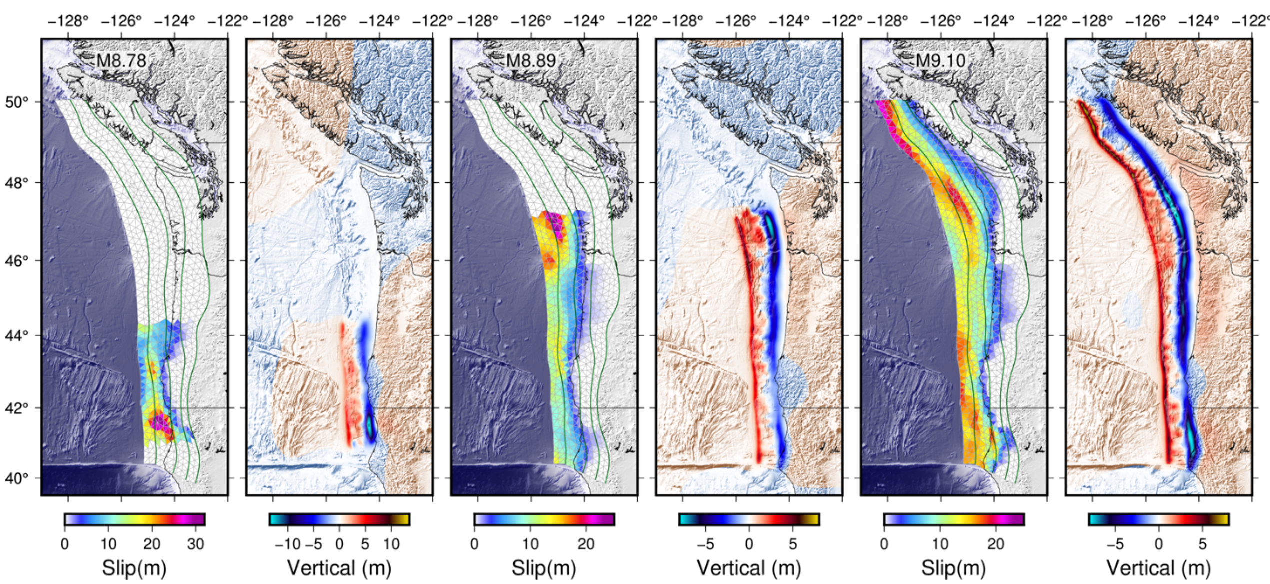

Figure 3. *Three examples of ruptures and their resulting vertical deformation of the seafloor used as the tsunami initial condition. The green lines are the 10km slab depth contours. The three events shown here are part of the set of events that match the tsunami amplitudes in Japan.*

The mean slip model, $\bar{\mu}$, is a critical parameter when using the KL expansion approach. Usually this is assumed to be a homogenous slip model with enough slip to match the desired target magnitude. Recently it has been shown that a heterogenous mean model can be used to introduce prior assumptions about the causative fault (Goldberg & Melgar, 2020). Extending this idea Small & Melgar (2020) have shown that it is possible to use assumptions about the geodetic locking in this way to condition the resulting ruptures. For the rupture simulations generated in this work we introduce five different assumptions (Figure 4) to capture all the proposed variability in the literature with respect to the down-dip edge of slip and the along-strike changes in fault locking of the CSZ. The "1cm" model reflects a common assumption that slip can only extend to the 1cm/yr slip deficit contour with no coseismic slip below that (Frankel et al., 2014, Wirth et al., 2018). This boundary is roughly at the coast or at the 15-20km slab depth contour. A second commonly assumed model is that slip can extend to the top of the slow slip region (Wirth et al., 2018). This is shown as the "Top SSE" mean model in Figure 4 and corresponds to depths that can reach ~30-40km. These two assumed mean models have no along-strike variability. As a result slip in the stochastic realizations is equally probable everywhere where $\mu \neq 0$. For the three other mean models we rely on known geodetic locking estimates for the CSZ. Two of them are the "Gamma" and "Gauss" models (Schmalzle et al., 2014) obtained from elastic block modeling. The third one we refer to as the "Li" model and was obtained from viscoelastic modeling (Li et al., 2018). These models have variable along-strike maximum depth, and also along-strike and along-dip variability in the strength of locking. As detailed by Small & Melgar (2020), by using the locking as the background mean model slip is not forced to have exactly the same pattern as the locking. Rather, areas with high locking will more frequently have high slip. Conversely areas with low locking will have large slip more infrequently. Utilization of these latter three mean models has the underlying assumption that the patten of locking prior to the 1700 earthquake, or sequence of earthquakes, was at least similar to what is seen today. The veracity of this assumption cannot be tested at present. For this reason we also include the 1cm and top of SSE models which minimize assumptions about the along-strike pattern of pre-1700 locking. In the end, the rupture models will be judged by their ability to fit the presumptive 1700 subsidence data.

For each of the 5 possible choices of mean model we generate 500 events for 0.1 magnitude unit bins between M8 and M9.5. This yields a total of 7,500 earthquakes for each of the assumed mean models and a total of 32,500 ruptures. We use a 1D layered Earth model for the CSZ (Melgar et al., 2016), so that the magnitude of each earthquake is affected by depth-dependent rigidity. It is important to note that we are not making a probabilistic hazard assessment so we do not follow Guttenberg-Richter statistics when deciding how many ruptures to generate at each magnitude bin. We are interested simply in exploring as much of the possible variability in behaviors, so we generate the same number of earthquakes for each bin. We use a mean rake of 90 corresponding to pure thrust but allow for small stochastic perturbations around this mean value (Graves & Pitarka, 2010). This yields small amounts of strike slip motion but the overall sense of motion remains pure thrust. In the stochastic rupture generation process it is not uncommon for the final magnitude to be slightly different from the design magnitude (Melgar et al., 2016). It is possible to rescale the slip to fit the target magnitude exactly. We have not done so here since we are not interested in exact magnitude values. As a result the final range of magnitudes in the 32,500 ruptures spans M7.8-M9.6 (Figure 2). An example of the resulting ruptures is shown in Figures 1 and 3. Figures S1-S4 also show 102 of the resulting ruptures across a wide variety of magnitudes. All the rupture models have been archived and can be downloaded for use. The ruptures are generated with a Python implementation of this stochastic approach which can also be obtained (see Data Availability Statement).

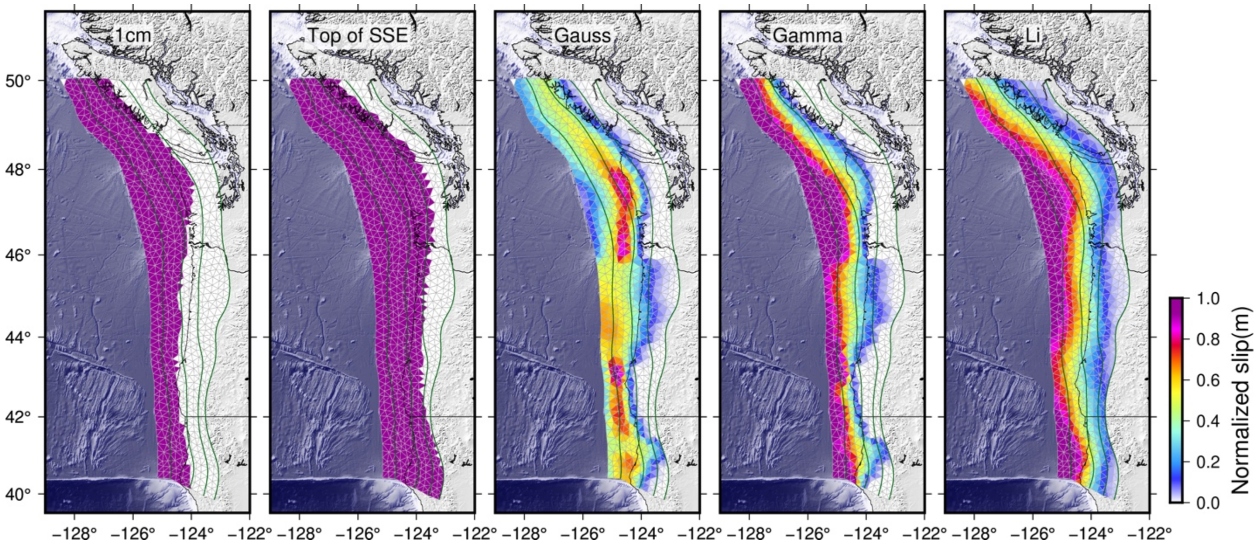

Figure 4. *The five mean models used for stochastic rupture generation. The green lines denote the 10km interval depth contours to the slab. The heterogenous models are the Gamma, Gauss and Li (Schmalzle et al, 2014, Li et al., 2018). The 1cm, and Top of SSE models assume homogenous locking with a hard down-dip cutoff depth (Wirth & Frankel, 2018)*

In a final step for each of the ruptures we calculate the coseismic deformation across a large regional domain (Figure 3). This is later used as the initial condition for tsunami modeling. We also calculate the vertical deformation at the coast at 2 km intervals (e.g. Figure 1B) and use it to estimate whether a specific rupture fits the geologic estimates of coastal subsidence or not.

2.2 Paleogeodetic subsidence estimates

There are three somewhat recent compilations pf paleogeodetic subsidence estimates for the CSZ. Leonard et al. (2010) (Figure 5) compiled subsidence estimates from a wide variety of sources published between 1988 and 2008 which are of highly variable quality. They include both stratigraphic and microfossil-based estimates of subsidence and overall have a larger uncertainty. Following that work improvements introduced mainly from paleoclimate techniques have allowed for better reconstructions of relative sea level rise (RSL) from foraminiferal transfer functions. This new approach was used to produce the database of Wang et al. (2013) which has overall lower uncertainty. Further statistical improvements in microfossil-based techniques has led to the Bayesian Transfer Function (BTF) approach which allows for the introduction of prior information into the RSL reconstructions and better modeling of the complexities of foraminifera species along the intertidal gradient. This newer approach was used by Kemp et al. (2018) (Figure 5) who reanalyzed the data from Wang et al. (2013) .

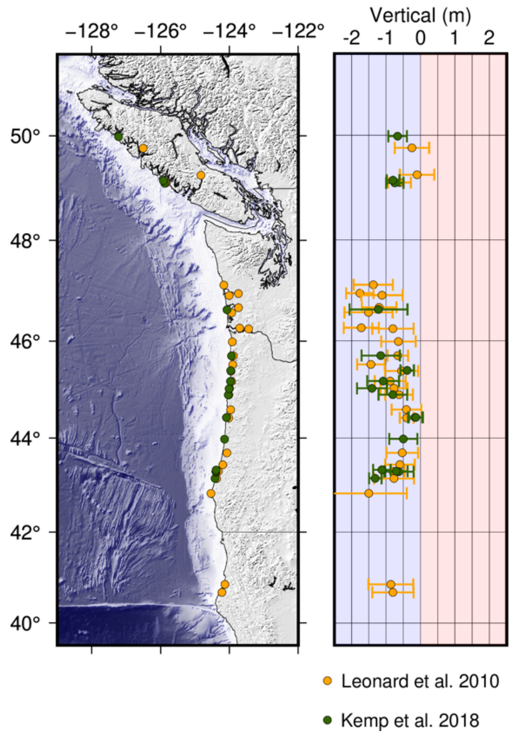

Figure 5. *Paleogeodetic subsidence estimates and uncertainties from Leonard (2010) and Kemp et al. (2018)*

Given these improvements we consider the BTF Kemp et al. (2018) data to be authoritative over older estimates. However, although all the databases overlap significantly in terms of the locations they cover, the lower uncertainty Kemp et al. (2018) dataset has no subsidence estimates in Northern California. As a result, we have kept the two larger uncertainty Northern California estimates from Leonard et al. (2010) and aggregated them into larger set of data points (Figure 1B).

Not all of the paleogeodetic points are exactly at the coastline. Many are a few kilometers inland in marshes and bays. While we calculate the coastal subsidence for each rupture model at 2 km intervals along the coast and use that for plotting, we also calculate the subsidence at the formal location of each geologic estimate. This latter set of points that is used when evaluating the ability of a particular rupture model to fit the data. As a measure of this misfit we use the root mean square (RMS) between modeled subsidence and geological observations.

It is important to note that we have assumed, as is commonly done, that the paleogeodetic estimates represent the coseismic subsidence strictly. However, rapid post-seismic motion immediately following an earthquake, whether in the form of afterslip on the same fault or viscoelastic relaxation of the mantle is common. It generally, although not always, follows the same sign as the coseismic offset, i.e. it would increase the subsidence or uplift signal, typically by ~10%. As a result, while the BTF methodology reduces the overall uncertainty of the subsidence estimations, an unknown amount of epistemic uncertainty from potential post-seismic processes remains. There is at present no way to separate the microfossil response from any potential post-seismic land level change from the strictly coseismic one.

2.3 Tsunami modeling and historical observations from Japan

For tsunami modeling we use the vertical coseismic deformation from each rupture as the initial condition (Figure 3) for propagation modeling. We disregard secondary deformation sources such as submarine landslides, splay faulting, or plastic deformation at the shallow wedge. Where, and how frequently these extra sources of tsunami energy would contribute during a CSZ earthquake is not known so it is very challenging to systematically model them. However, they would all serve to increase tsunami amplitudes (Gao et al., 2018, Ma & Nie, 2019). As a result, including any of these extra sources of tsunamigenesis would buttress our findings further by allowing even smaller magnitude events to replicate the tsunami amplitudes in Japan.

Following definition of the seafloor initial condition, we use the finite volume depth-averaged code GeoClaw (Berger et al., 2011). This solves the two-dimensional non-linear shallow water equations on a sphere and can deal with discontinuities in the solution, such as turbulent bore formation, by shock capturing. It employs adaptive mesh refinement (AMR) such that regions of larger tsunami complexity are automatically refined to higher discretization levels according to heuristics prescribed by the user.

The trans-Pacific model domain is shown in Figure 1C and Animation S1. We use three bathymetry grids that span six levels of refinement (Table S1). For propagation in the open ocean in deep water we use the ETOPO1 1 arcmin grid (Amante et al., 2001) which is used for AMR levels 1-3 and spans the entire domain. Around the Japan archipelago we use SRTM15+ grid, which includes both topography and bathymetry and is sampled at 15 arcsec for AMR level 4 (Tozer et al., 2019). For the five historical locations where high resolution modeling is required we combine the M7000 multibeam gridded bathymetry purchased from the Japanese Hydrographic Association (Figure 1C) and the SRTM1 1 arcmin digital elevation model (Farr et al., 2007). For each of the five locations in Japan where there are historical estiamtes of tsunami amplitude (Satake et al., 2003) we specify a 20x20km box around each site and allow refinement down to AMR level 5 (5 arcsecs) and AMR level 6 (1 arcsec) using these finer grids.

We ran the propagation models for 20 hrs of model time. Time-stepping is variable and numerical stability is ensured using the Courant-Friedrichs-Lewy condition which was set at 0.75. Geoclaw is suitable for near shore inundation analysis. It employs a Manning-type law for bottom friction (we held the coefficient fixed at 0.025) and has a moving sea/land boundary condition that allows cells to be wetted or dried as the simulation progresses. It also has a non-reflecting outflow boundary condition at the edges of the model domain.

Since rupture propagation velocities are much faster than tsunami wave velocities, we assume instantaneous coseismic deformation as the initial condition for tsunami modeling. This assumption has a negligible effect on near-source modeling but can, in special cases, such as when ruptures are very long and extremely unilateral, rotate the main beam of tsunami radiation in the direction of rupture propagation (Williamson et al., 2019). Accounting for this finite duration in the tsunami initial condition is possible at the expense of a significant slow-down in the computation times because it requires very short time steps to be taken as the rupture propagates. it is possible that for a particular rupture this can rotate more tsunami energy towards or away from Japan. However since we are relying on the aggregate results of tens of hundreds of tsunami simulations we assume that over the ensemble of simulations this effect will average out. After all, strongly unilateral ruptures are less common than bilateral ones (Melgar & Hayes, 2019). As a test of this Figure S5 shows a tsunami modeled with an instantaneous source and considering south to north and north to south finite duration sources. We find no evidence of a strong effect in Japan.

GeoClaw includes Coriolis forcing, which can have a small impact at transoceanic distances, and it is not at present capable of modeling the dispersive nature of tsunami propagation. Dispersion can have a measurable effect in the estimated arrival times of tsunami waves at trans-oceanic distances. However, for inundation and coastal amplitudes the non-linear propagation, especially in shallow water with complex bathymetry (which GeoClaw can model well), is of far larger importance (Glimsdal et al., 2013).

In order to assess if a specific tsunami model reflects the historical observations we use the dataset of tsunami amplitudes in Japan from Satake et al. (2003) (shaded regions in Figure 2D, Table S2). These include corrections for tides and land-level changes. The values represent the expected amplitude of the tsunami at the shoreline, not inland where damage was reported or observed. To obtain these reconstructed values a number of different assumptions can be made and which yield a range of possible tsunami amplitudes. For example, the lower amplitude values assume that water depth at inland locations, were damage was observed, are the same as the amplitude at the coastline. This is generally considered a conservative approach. Meanwhile if the tsunami is assumed to have a larger amplitude at the coastline than at inland sites it is necessary to tailor the correction to each site. This was done by using the 1960 Chile earthquake as a calibration event. This second set of amplitudes generally yields larger amplitudes than the more conservative one. For each of the five historical locations we extracted tsunami output on regular grids spanning 5km around the point of interest and, similar to what was done originally by Satake et al. (2003) we kept the coastal amplitude with the largest value within 1 km of each site as the tsunami amplitude at that location and for that particular event. We note that at the Nakaminato site only a single amplitude value is reported as ~1m with no specified range. We use an uncertainty of +/- 0.5m at this location based on a similar range of values at Miho, the other low amplitude location.

3. Results

3.1 Rupture models and fits to the coastal subsidence data

Figures 2A,2B. shows the statistics of the rupture dimensions and slip for all the earthquakes. The mean values follow known scaling laws, but variability is allowed; two events of the same magnitude can and will have different dimensions and slip distributions. For example M9 ruptures as short as ~300km are uncommon but possible and they can also extend to saturate the entire length of the plate boundary. Further examples of this variability can be seen in Figure 3 and S1-S4.

For each of the 32,500 ruptures we calculate the root mean square (RMS) misfit between the predicted coastal deformation and the paleogeodetic subsidence observations constructed by aggregating two databases of measurements as described in Section 2.2. To obtain the RMS we only consider paleogeodetic points within 50km of the surface projection of the polygon that circumscribes each rupture. For instance, for the rupture in Figure 1A, the two southernmost paleogeodetic measurements do not contribute to the misfit since they are further than 50km from the part of the megathrust that slips. The idea is to evaluate an event's ability to replicate its "local" pattern and not penalize it for not fitting the margin-scale distribution. Earthquakes that rupture only a portion of the plate boundary will have near-zero deformation at large distances which would unnecessarily increase the RMS misfit. This is done in anticipation that it might be possible to fit the entire margin-scale distribution by summing the contributions from many ruptures.

Figure 1C shows the distribution of RMS misfits as a function of magnitude with this 50 km rule applied. We set an RMS threshold cutoff of 0.4 m and keep 1,635 ruptures that fit this criterion. We consider this subset of events for later tsunami modeling. Any RMS cutoff will be arbitrary, but this threshold is equivalent to the mean uncertainty in the coastal subsidence estimates (Figure 1B) and segregates out ~5% of the ruptures from the dataset as "high-quality" models. The ruptures in Figures 1A,3 and S1-S4 are all examples from this high quality subset of events.

3.2 Rupture models that match the far field tsunami

For the subset of 1,635 events described in the previous section, we also calculate regional seafloor deformation (Figure 3) and use it as the initial condition for trans-Pacific hydrodynamic modeling (Section 2.3). Figure 1C shows an example tsunami model from the rupture in Figure 1A. The inset shows the maximum amplitudes across the Pacific. It is interesting to note that tsunami energy is not predominantly directed towards Japan but rather towards Hawaii and the Emperor islands. This is a common feature of all Cascadia tsunami models and suggests Hawaii would more effectively record the paleotsunami history of the region. We are not aware of any observations there. Animation S1 however shows that significant tsunami energy can make it to Japan from complex propagation paths such as reflections of the Hawaiian islands and through wave channeling across the Alaskan and Kurile trenches. Indeed, this latter path through the deep water of the subduction trenches seems to consistently provide the first arrivals to Japan.

Shown in Figure 1C as well are examples of the maximum tsunami amplitudes in Japan at all 6 historical locations (note that two are very close to each other, Kuwagasaki and Tsugaruishi). The detailed bathymetry contours and topography are shown as well. We generally observe that amplitudes decay from North to South across Honshu, this is readily explained because the great circle path between Cascadia and Japan places the southern reaches of the island further away from the CSZ. The exception is Tanabe which is further south but consistently has slightly larger amplitudes than Miho. Likely from some contribution of local amplification.

Figure 2D shows a summary of the distributions of amplitudes at each location from the 1,635 high quality ruptures disaggregated into 5 magnitude bins. We consider that a tsunami model for a particular earthquake “fits” the historical data when the amplitudes at all 5 locations are within the range of values inferred to have occurred in 1700 by Satake et al. (2003). 102 events (shown in Figures S1-S4) fit this criterion. The histogram in Figure 1E shows that these are all in the M8.7 to M9.2 range. We also find 483 events in the M7.8 to M8.6 range that have amplitudes smaller than 30 cm at all the five locations. Minor tsunami damage typically begins at > 0.5 m amplitudes and quickly escalates in intensity after 1.5 m (Whitmore et al., 2008). Very rarely, if ever, is damage observed for amplitudes below 30 cm. As a result these 483 events represent earthquakes that fit their local subsidence pattern in Cascadia but can be reasonably assumed as generating tsunamis that are very unlikely to be of sufficient import to be in the historical record from Japan.

3.3 Clustering ruptures into event sequences

The process outlined above yields two sets of earthquakes. Both fit their local coseismic subsidence patterns in the CSZ, while only one of them generates a tsunami big enough to be likely in Japanese historical records. Previous work disregarded earthquake models that did not simultaneously fit the tsunami and the paleogedetic data across the entire margin (e.g. Satake et al., 2003). Here we relax this assumption and pose the simple question: is it possible to combine earthquakes in such a way that one event from the large tsunami event set and one or many from the small tsunami event set can simultaneously explain all the observations? To answer this we systematically explore all combinations of events subject to the following restrictions (i) only one event from the set that fits the tsunami in Japan can be used (ii) between 0 and 4 events from the set that has a tsunami <30 cm in Japan can be used (iii) there can be no more than 10% overlap in terms of the rupture area between all the events and (iv) the combined coastal subsidence pattern between all events must fit the margin-wide paleogeodetic data to the same RMS < 0.4 m level.

As a result of these heuristics we can form an event sequence with only one event (N=1) or as many as five total earthquakes (N=5). Figure 6 shows specific examples of ruptures for sequences for this range of possibilities. Figure 6A, shows a single M9.1 event that spans the entire plate boundary and can still be invoked to fit all the data. However, Figures 6B-E show that a sequence with many events can fit the data to the specified RMS misfit as well. A mainshock that spans less than half the length of the subduction zone, and generates the tsunami in Japan is possible (more examples are in Figures S1-S4), and a wide variety of other behaviors occur. Figure 6B shows that indeed the full plate boundary, with no gaps, can be filled with just two events. But, because there are spatial voids in the paleogeodetic data, it is also possible to leave portions of the megathrust unbroken and match the subsidence pattern (Figures 6C-E). Given that at present high locking is estimated everywhere on the megathrust (Schamzle et al., 2016, Li et al., 2018) this is a previously unconsidered and worrying proposition for CSZ hazards. Our modeling suggests it is possible that some smaller segment or segments of the megathrust did not break in the last event or sequence of events and have been accumulating a slip deficit for at least two earthquake cycles. Most strikingly, it is also possible (Figures 6C and 6D) that the subsidence at the locations of the 1699 trees, previously used as hard proof of a single plate-boundary event (Yamaguchi et al., 1997, Atwater et al., 2005) not even be associated with the mainshock at all but be produced by a smaller event instead.

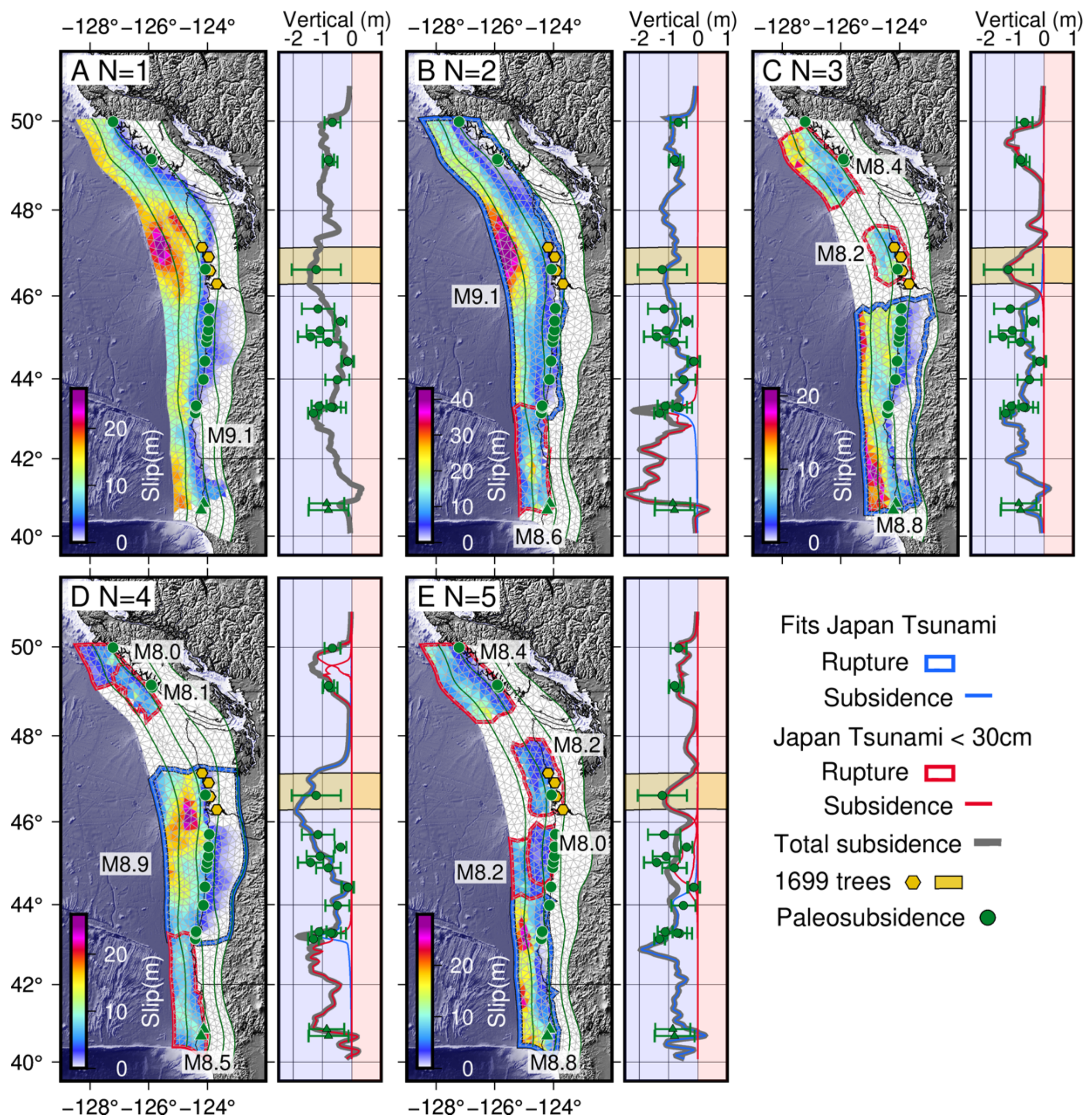

Figure 6. *Example earthquake sequences with one (A) or many (B)-(E) earthquakes. Each panel shows the slip distributions and predicted coseismic subsidence patterns for the individual earthquakes as well as from the combination of them. The green lines denote the 10km depth contours for the slab geometry. Shown as well are the locations and values of paleogeodetic subsidence estimates as well as the locations of the trees inferred to have subsided between 1699 and 1700.*

Figure 6 shows specific examples of event sequences but there are thousands of potential combinations and the complexity in how earthquakes can be combined increases rapidly with the number of allowed earthquakes. Figure 7 shows a summary of all the possible combinations when applying the event selection heuristics. We find that 9 plate-boundary scale earthquakes with M8.9 to M9.2 fit all the possible observations at the CSZ and in Japan without needing to involve events from the small tsunami dataset (N=1). However, because there are many large (M>8.7) earthquakes that only rupture a portion of the plate boundary (Figure 3,6,S1-S4) it is possible to fit the data, given the restrictions outlined above, with multiple ruptures as well. While the lower bound of the "mainshock" is never less than M8.8, for most of the permutations of event groupings that fit all the observations, as the number of earthquakes increases to two (N=2) or more, the higher magnitude events are less favored. Similarly, as the number of events in the sequence increases, lower magnitude events are required. For N=4 and N=5, events with magnitudes as low as M8 become quite common. It is possible to continue exploring sequences with more than 5 earthquakes, as we have done here, however, the number of permutations of events grows rapidly and this becomes a computationally intensive task. With just the two sets of earthquakes we have used here, by the time N=5 there are $5x10^{12}$ possible combinations that need to be examined of which over 1 million fit both the paleogeodetic data and the tsunami in Japan.

Discussion

4.1 Characteristics and implications of the event sequences

We have defined the "mainshock" as the larger magnitude event that is potentialy responsible for the tusnami in Japan. In none of the sequences (Figures 6,7) is the mainshock ever smaller than the secondary earthquakes. In order to explain the tsunami in Japan we still require a large (M8.7-M9.2) event to occur on the CSZ on January 26th 1700. However, this requirement is now only strongly constrained by the historical documents from Japan (Satake et al., 2003) and not necessarily by the 1699 trees, as has commonly been argued (e.g. Atwater et al., 2005). In Section 3.3 we showed it is possible for the mainshock to produce no coseismic deformation at the location of the 1699 trees. This is the only location with very tight age constraints on coseismic deformation. Age estimates of subsidence (Figure 1) at other locations along the margin have uncertainties that are at best several decades and more frequently several centuries. This is still too coarse to favor the hypothesis that a single event produces the paleogeodetic subsidence over the multi-event one. With this in mind, the view that the CSZ has two distinct modes (Frankel et al., 2014) where it either fails in a single large ~M9 event or in many smaller events is also likely incomplete. As we have shown, these modes are not mutually exclusive, following known earthquake scaling laws, it is possible to have an ~M9 rupture on only a portion of the plate boundary. This mainshock can then be either preceded or followed by one or many ruptures in the ~M8.0-M8.6 range.

The timing of individual events in the potential sequences is difficult to ascertain at present. High resolution C14 dates that place the subsidence in the 1690 to 1720 interval only exist for Northern California and Southern Washington, and the locations of the 1699 trees is limited to a ~100km stretch of southern Washington. C14 dating of bulk peat samples elsewhere (Oregon and British

Columbia) provide only lower resolution estimates for the subsidence. So, while it is more likely that an event sequence that includes the 1700 mainshock spans just a few decades around that date, that it spans as much as a century, especially before 1700, cannot be ruled out. Further efforts to fill paleogeodetic data gaps and to date, with high resolution, the timing of subsidence will do much to elucidate the likely sequencing of the events or prove conclusively that a single through-going earthquake is needed. There are significant challenges for this. It is difficult to identify locations at the present paleogeodetic data gaps (Figure 1A) where salt marshes exist that have reliable microfossil records where the BTF approach can be applied (Walton et al., 2021). Additionally, the kind of dendrochronological work that allows dating with resolution of one year is made challenging by the habitat distribution of western red cedar trees. Also, it requires a fortunate set of circumstances were a living witness tree, unaffected by the subsidence and tsunami, can be found close to a deceased tree that retains enough unweathered material for dating (Atwater et al., 2005). Nonetheless the results shown here argue efforts on both of these fronts, as well as applying new techniques, should be renewed.

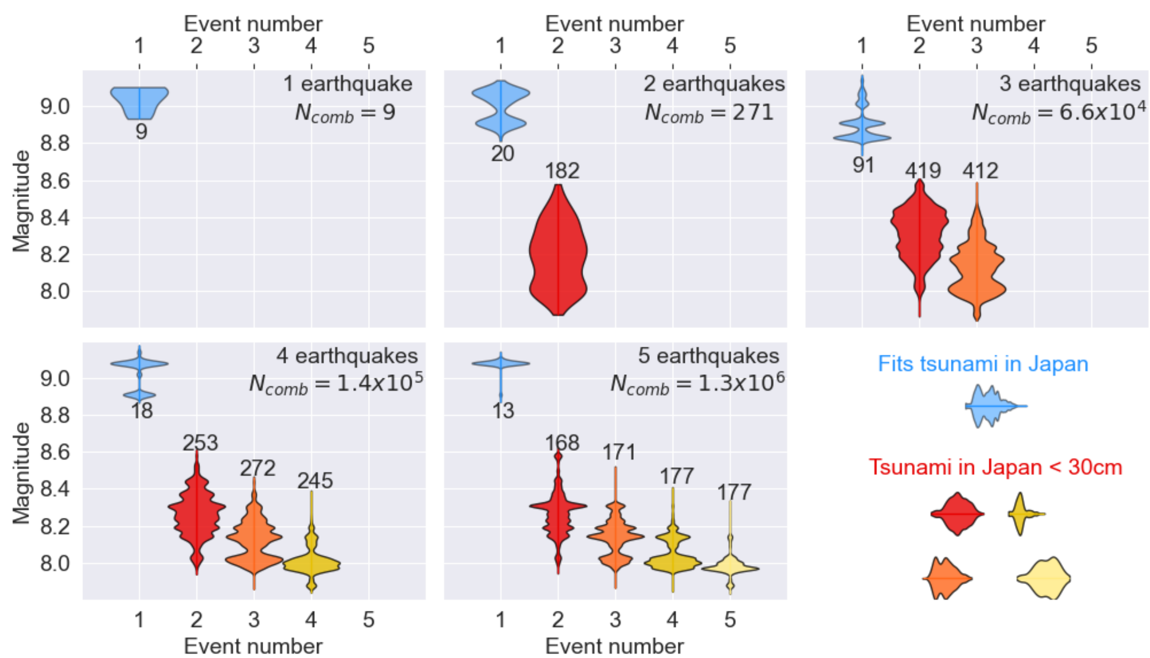

Figure 7. *Violin plots showing the distributions of potential earthquake sequences that together fit both the CSZ subsidence data and the tsunami in Japan. Each panel shows the possible sequences that group between one and five earthquakes. The blue violins indicate the magnitude distribution of events that fit the tsunami in Japan, the red to yellow violins show the magnitude distribution of events that produce tsunamis smaller than 30cm in Japan. For each event grouping the RMS misfit to the CSZ subsidence is less than 0.4 m. N_{comb} is the total number of combinations of events that satisfy the heuristics for forming a sequence. The number above or below each violin shows the number of unique earthquakes for that distribution.*

Faced with this potential complexity it is tempting to invoke Occam's razor in favor of the single event model. However, it has been shown that, even though they are possible, large throughgoing ruptures are less likely at megathrusts, like the CSZ, with significant along-strike curvature (Bletery et al., 2016). Additionally, there are recent examples of large swaths of a megathrust failing in a sequence spanning years to decades. The 2004 M9.2 Sumatra earthquake was quickly followed by the 2005 M8.7 Nias and 2007 M8.5 Bengkulu earthquakes immediately south of it (Banerjee et al., 2007; Gusman et al., 2010). Similarly, the slip distribution for the great 1960 M9.5 Valdivia, Chile earthquake abuts, and might even have some limited overlap, with the 2010 M8.8 Maule event (Lorito et al., 2010). This 50 yr separation between events is similar to what is possible in the CSZ given present dating estimates of coastal subsidence. Counterexamples exist of course, as the 2011 M9 Tohoku-oki earthquake (Ozawa et al., 2011) has not yet been followed by another large M8+ rupture elsewhere on the megathrust.

4.2 Why were multi-event sequences considered unlikely before?

One of the interesting findings from the models is that ruptures that are surprisingly short and span as little as ~40% of the plate boundary (Figures 3, S1-S4) can still generate a tsunami of sufficient amplitude in Japan. This is in stark contrast to previous modeling results from Satake et al. (2003) who found that only ruptures approximating plate-boundary length generated significant enough tsunami. That finding has been used extensively in support of the single event model (Walton et al., 2021). This discrepancy warrants a brief discussion.

The slip distributions tested by Satake et al. (2003) are not quite homogenous but they have very limited variability. They have almost constant slip along dip with only a gentle taper with depth. This simple along-dip distribution is then extended along-strike. Slip heterogeneity observed in inversions is much more drastic than this (e.g. Hayes, 2017). Melgar et al. (2019) compared the tsunamigenic potential of homogenous and heterogenous slip models while holding the fault dimensions, Earth structure model, and earthquake magnitude fixed. The comparison showed that the simple act of redistributing slip from homogenous into heterogenous produces as much as half an order of magnitude difference in the tsunami potential energy. This is by virtue of the non-linear relationship between slip and energy. High-slip asperities end up having an outsized contribution to the energy budget that is not offset by energy losses from low-slip regions. This likely contributes to the reduced dimension models from Satake et al. (2003) not having enough amplitude in Japan.

However, this is not the complete explanation. Figure 8A shows the tsunami potential energy for both the ruptures that match the tsunami amplitudes in Japan and those that do not. We find that there is a 1.5 order of magnitude range of possible energies, and yet the range of amplitudes in Japan (Figure 2D) varies by at most a factor of 2. How can this large energy variation produce only modest changes in the far-field tsunami? The answer is that due to the complex propagation path there is a large variability in how efficiently tsunami energy from different parts of the CSZ travels to Japan. Figure 8B,C shows homogenous slip M8.6 earthquakes located at different positions along-strike and their resulting tsunami amplitudes. Tsunamis generated in the southern half of Cascadia produce amplitudes almost five times as large in Japan than tsunamis generated offshore Vancouver Island. Indeed Figures (S1-S4) show that short length events that replicate the tsunami in Japan are almost exclusively located south of 46°N. These two factors, slip heterogeneity, and varying along-strike sensitivity of the far-field tsunami, can explain why simplified slip models tested previously were ruled out.

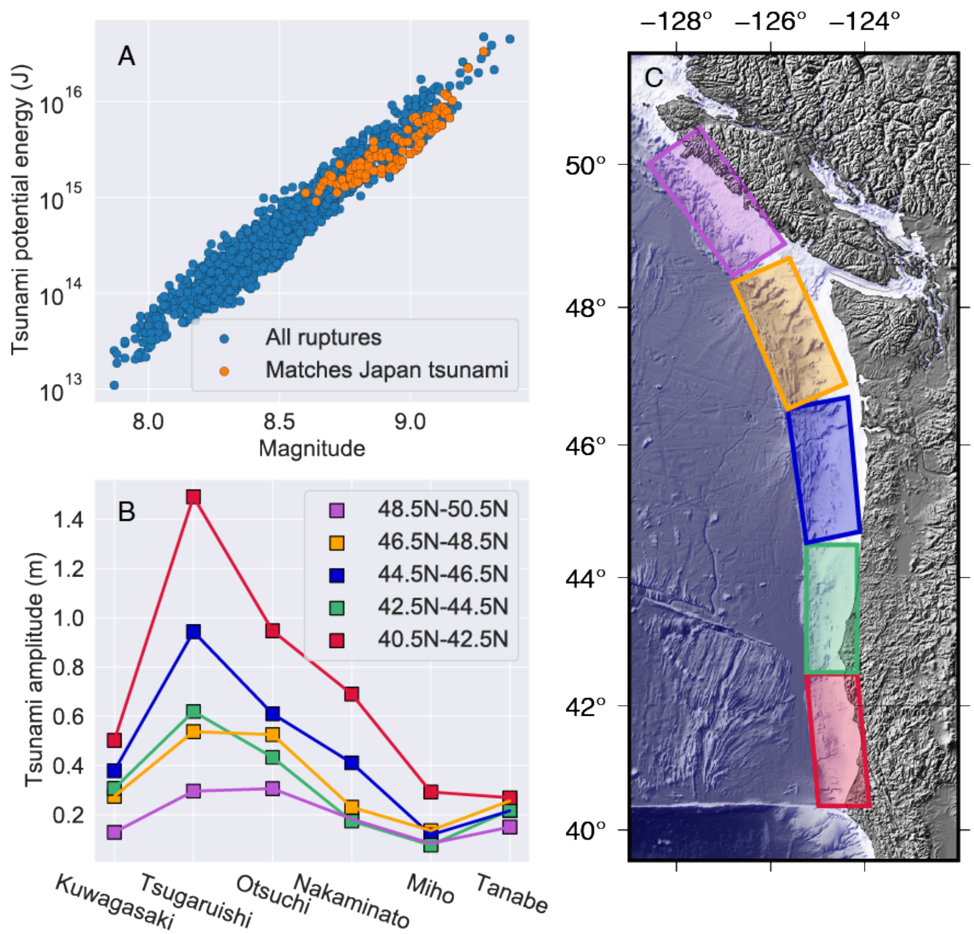

Figure 8. *(A) Initial tsunami potential energy for the 1,635 modeled tsunamis (blue) and for the 102 tsunami that match the historical amplitudes from Japan (orange). (B) Tsunami amplitudes in Japan as a function of location of slip on the CSZ. (C) Locations of five different M8.6 earthquakes all with homogenous slip used for tsunami propagation to obtian the values in (B)*

4.3 Other geological constraints

There are other geological observations which could potentially contribute to distinguishing between the single event and the multi-earthquake sequence hypothesis. One of them is turbidite deposits identified in offshore cores. The challenge there is that the dating if the deposits is still quite coarse and of the order of a few centuries (Goldfinger et al., 2012). Additionally, what level of shaking is required to trigger a turbidity current is at present not well understood. There is evidence that weak shaking can be enough to trigger some turbidites (e.g. Johnson et al., 2017). So while correlation across long distances of turbidities can suggest margin-scale failures, here too, that they are produced by smaller magnitude events spanning decades cannot be ruled out.

Perhaps one promising avenue is to use the locations of tsunami sand sheets identified at coastal locations (Atwater et al., 1995; Walton et al., 2021). These are often inside bays and estuaries many kilometers from the coast. Using high-resolution bathymetry, topography, and hydrodynamic modeling they could potentially be used to discriminate between potential rupture models. It is not energetically favorable for a tsunami to travel long distances in very shallow water. So, tsunami deposits with long run-up distances are thought to correlate with large magnitude or high shallow slip events (e.g. Ramirez-Herrera et al., 2020).

4. Conclusions

The notion that only a single plate-boundary spanning earthquake occurring in January 26th, 1700 can explain the set of geological and historical observations is the prevailing view in CSZ science (Walton et al., 2021). Here we have revisited this issue using modern rupture and tsunami propagation modeling approaches. We find that indeed, it is possible to invoke a single event to explain the observations. However, we also show that a multi-event sequence explains the data just as well. In the multi-earthquake sequence model, a mainshock with M>8.7 occurring on January 26th 1700 is still required to explain the tsunami in Japan. However, we have also shown that this mainshock could rupture as little as ~40% of the plate boundary. As many as four more smaller (M<8.6) events can then be invoked to fill in most of the megathrust and explain the margin-scale subsidence signal. These smaller events do not make a tsunami large enough to be recorded in Japan. We also find that due to the gaps in coastal subsidence observations it is possible for some segments of the megathrust to have remained unbroken for at least 2 earthquake cycles. We cannot at present say much about the timing of earthquakes in such a sequence due to the uncertainties in the age estimates of coastal subsidence. Our findings argue strongly that the prevailing single-event model cannot be thought of as better justified by the observations than the multi-earthquake sequence model. This has important implications for Cascadia geodynamics and for how earthquakes hazards for the region are quantified.

Acknowledgments

I have benefitted from many discussions with colleagues on Cascadia earthquake science, paleoseismology, and rupture and tsunami modeling, special thanks to Loyce Adams, Brian Atwater, Bryan Black, Frank Gonzalez, Andrew Kemp, Randy LeVeque, Lydia Staisch, Jason Padgett, Josh Roering, Valerie Sahakian, Will Struble, Amanda Thomas, Maureen Walton, Amy Williamson, and Erin Wirth. Special thanks to Soli Garcia whose help was invaluable for securing the Japan bathymetry data. This work was partially funded by NASA grants 80NSSC19K1104 and 80NSSC19K0360 and NSF grant .

Data Availability Statement

The 32,500 rupture models are available on Zenodo (Melgar, 2020a). The stochastic rupture modeling code is on Zenodo (Melgar 2020b) and available on GitHub (https://github.com/dmelgarm/MudPy). GeoClaw, the tsunami modeling code is archived at Zenodo (Mandli et al., 2017) and available at http://clawpack.org

References

Allen, T. I., & Hayes, G. P. (2017) Alternative rupture-scaling relationships for subduction interface and other offshore environments. Bulletin of the Seismological Society of America, 107(3), 1240-1253.

Amante, C., & Eakins, B. W. (2001) ETOPO1 1 Arc-minute global relief model: procedures, data sources and analysis. NOAA Technical Memorandum NESDIS NGDC-24. National Geophysical Data Center, NOAA, 10, V5C8276M.

Atwater, B.F., (1987). Evidence for great Holocene earthquakes along the outer coast of Washington State. Science, 236(4804), pp.942-944.

Atwater, B.F. and Yamaguchi, D.K. (1991) Sudden, probably coseismic submergence of Holocene trees and grass in coastal Washington State. Geology, 19(7), pp.706-709.

Atwater, B.F., Nelson, A.R., Clague, J.J., Carver, G.A., Yamaguchi, D.K., Bobrowsky, P.T., Bourgeois, J., Darienzo, M.E., Grant, W.C., Hemphill-Haley, E. and Kelsey, H.M. (1995) Summary of coastal geologic evidence for past great earthquakes at the Cascadia subduction zone. Earthquake spectra, 11(1), pp.1-18.

Atwater, B. F., Satoko, M. R., Kenji, S., Kazue, U., Yoshinobu, T., & Yamaguchi, D. K. (2005). The orphan tsunami of 1700: Japanese clues to a parent earthquake in North America (No. 1707). US Geological Survey.

Banerjee, P., Pollitz, F., Nagarajan, B., & Bürgmann, R., (2007) Coseismic slip distributions of the 26 December 2004 Sumatra–Andaman and 28 March 2005 Nias earthquakes from GPS static offsets. Bulletin of the Seismological Society of America, 97(1A), S86-S102.

Bartlow, N. M. (2020). A long-term view of episodic tremor and slip in Cascadia. Geophysical Research Letters, 47(3), e2019GL085303.

Berger, M. J., George, D. L., LeVeque, R. J., & Mandli, K. T. (2011). The GeoClaw software for depth-averaged flows with adaptive refinement. Advances in Water Resources, 34(9), 1195-1206.

Blaser, L., Krüger, F., Ohrnberger, M., & Scherbaum, F. (2010) Scaling relations of earthquake source parameter estimates with special focus on subduction environment. Bulletin of the Seismological Society of America, 100(6), 2914-2926. (2010)

Bletery, Q., Thomas, A. M., Rempel, A. W., Karlstrom, L., Sladen, A., & De Barros, L. (2016) Mega-earthquakes rupture flat megathrusts. Science, 354(6315), 1027-1031, (2016).

Farr, T. G., Rosen, P. A., Caro, E., Crippen, R., Duren, R., Hensley, S., ... & Seal, D. The shuttle radar topography mission. Reviews of geophysics, 45(2). (2007)

Frankel, A., Chen, R., Petersen, M., Moschetti, M., & Sherrod, B. (2015) 2014 update of the Pacific Northwest portion of the US National Seismic Hazard Maps. Earthquake Spectra, 31(S1), S131-S148.

Frankel, A., Wirth, E., Marafi, N., Vidale, J., & Stephenson, W. (2018) Broadband Synthetic Seismograms for Magnitude 9 Earthquakes on the Cascadia Megathrust Based on 3D Simulations and Stochastic Synthetics, Part 1: Methodology and Overall Results, Methodology and Overall Results. Bulletin of the Seismological Society of America, 108(5A), 2347-2369.

Gao, D., Wang, K., Insua, T. L., Sypus, M., Riedel, M., & Sun, T. (2018). Defining megathrust tsunami source scenarios for northernmost Cascadia. Natural Hazards, 94(1), 445-469.

Glimsdal, S., Pedersen, G. K., Harbitz, C. B., & Løvholt, F. Dispersion of tsunamis: does it really matter? (2013).

Goldberg, D. E., & Melgar, D. Generation and validation of broadband synthetic P waves in semistochastic models of large earthquakes. Bulletin of the Seismological Society of America, 110(4), 1982-1995. (2020).

Goldfinger, C., Nelson, C. H., Morey, A. E., Johnson, J. E., Patton, J. R., Karabanov, E. B. & Enkin, R. J. (2012) Turbidite event history—Methods and implications for Holocene paleoseismicity of the Cascadia subduction zone (No. 1661-F). US Geological Survey.

Graves, R. W., & Pitarka, A. Broadband ground-motion simulation using a hybrid approach. Bulletin of the Seismological Society of America, 100(5A), 2095-2123. (2010).

Gusman, A. R., Tanioka, Y., Kobayashi, T., Latief, H., & Pandoe, W. (2010) Slip distribution of the 2007 Bengkulu earthquake inferred from tsunami waveforms and InSAR data. Journal of Geophysical Research: Solid Earth, 115(B12).

Hayes, G. P. (2017), The finite, kinematic rupture properties of great-sized earthquakes since 1990. Earth and Planetary Science Letters, 468, 94-100.

Hayes, G. P., Moore, G. L., Portner, D. E., Hearne, M., Flamme, H., Furtney, M., & Smoczyk, G. M., (2018) Slab2, a comprehensive subduction zone geometry model. Science, 362(6410), 58-61.

Heaton, T. H., & Hartzell, S. H. (1987) Earthquake hazards on the Cascadia subduction zone. Science, 236(4798), 162-168.

Johnson, H. P., Gomberg, J. S., Hautala, S. L., & Salmi, M. S. (2017). Sediment gravity flows triggered by remotely generated earthquake waves. Journal of Geophysical Research: Solid Earth, 122(6), 4584-4600.

Kelsey, H. M., Witter, R. C., and Hemphill-Haley, E. (2002) Plate-boundary earthquakes and tsunamis of the past 5500 years, Sixes River estuary, southern Oregon, Geological Society of America Bulletin 114, 298–314.

Kemp, A. C., Cahill, N., Engelhart, S. E., Hawkes, A. D., & Wang, K., (2018) Revising Estimates of Spatially Variable Subsidence during the AD 1700 Cascadia Earthquake Using a Bayesian Foraminiferal Transfer Function. Bulletin of the Seismological Society of America, 108(2), 654-673, (2018)

Leonard, M. (2010) Earthquake fault scaling: Self-consistent relating of rupture length, width, average displacement, and moment release. Bulletin of the Seismological Society of America, 100(5A), 1971-1988.

Leonard, L. J., Currie, C. A., Mazzotti, S., & Hyndman, R. D. (2010) Rupture area and displacement of past Cascadia great earthquakes from coastal coseismic subsidence. GSA Bulletin, 122(11-12), 2079-2096.

LeVeque, R. J., Waagan, K., González, F. I., Rim, D., & Lin, G. (2016) Generating random earthquake events for probabilistic tsunami hazard assessment. In Global Tsunami Science: Past and Future, Volume I (pp. 3671-3692). Birkhäuser, Cham.

Li, S., Wang, K., Wang, Y., Jiang, Y., & Dosso, S. E. (2018) Geodetically inferred locking state of the Cascadia megathrust based on a viscoelastic Earth model. Journal of Geophysical Research: Solid Earth, 123(9), 8056-8072.

Lorito, S., Romano, F., Atzori, S., Tong, X., Avallone, A., McCloskey, J. & Piatanesi, A. (2011) Limited overlap between the seismic gap and coseismic slip of the great 2010 Chile earthquake. Nature Geoscience, 4(3), 173-177.

Ma, S., & Nie, S. Dynamic Wedge Failure and Along-Arc Variations of Tsunamigenesis in the Japan Trench Margin. Geophysical Research Letters, 46(15), 8782-8790. (2019)

Mai, P. M., & Beroza, G. C., A spatial random field model to characterize complexity in earthquake slip. Journal of Geophysical Research: Solid Earth, 107(B11), ESE-10. (2002).

Mandli, K., et al. (2017). GeoClaw with Assimilation (Version 5.2.2.1-alpha). Zenodo. http://doi.org/10.5281/zenodo.1098738

McCaffrey, R., & Goldfinger, C. (1995) Forearc deformation and great subduction earthquakes: Implications for Cascadia offshore earthquake potential. Science, 267(5199), 856-859.

Melgar, D. (2020a). 2020 Cascadia rupture models [Data set]. Zenodo. http://doi.org/10.5281/zenodo.4300896

Melgar, D. (2020b). MudPy Version v1.2. Zenodo. http://doi.org/10.5281/zenodo.3703200

Melgar, D., & Hayes, G. P. (2019a) The correlation lengths and hypocentral positions of great earthquakes. Bulletin of the Seismological Society of America, 109(6), 2582-2593. (2019)

Melgar, D., Williamson, A. L., & Salazar-Monroy, E. F. (2019b). Differences between heterogenous and homogenous slip in regional tsunami hazards modelling. Geophysical Journal International, 219(1), 553-562.

Nelson, A.R., B.F. Atwater, P.T. Bobrowsky, L-A. Bradley, J.J. Clague, G.A. Carver, M.E. Darienzo, W.C. Grant, H.W. Krueger, R. Sparks, T.W. Stafford, Jr., and M. Stuiver, (1995) Radiocarbon evidence for extensive plate-boundary rupture about 300 years ago at the Cascadia subduction zone: Nature, v. 378, p. 371-374.

Nelson, A.R., Shennan, I. and Long, A.J. (1996) Identifying coseismic subsidence in tidal-wetland stratigraphic sequences at the Cascadia subduction zone of western North America. Journal of Geophysical Research: Solid Earth, 101(B3), pp.6115-6135.

Nelson, A. R., Kelsey, H.M., and Witter, R. C. (2006) Great earthquakes of variable magnitude at the Cascadia subduction zone, Quaternary Research 65, 354–365.

Nosov, M. A., Bolshakova, A. V., & Kolesov, S. V. (2014). Displaced water volume, potential energy of initial elevation, and tsunami intensity: Analysis of recent tsunami events. Pure and Applied Geophysics, 171(12), 3515-3525.

Ozawa, S., Nishimura, T., Suito, H., Kobayashi, T., Tobita, M., & Imakiire, T. (2011) Coseismic and postseismic slip of the 2011 magnitude-9 Tohoku-Oki earthquake. Nature, 475(7356), 373-376. (2011)

Ramírez-Herrera, M. T., Corona, N., Cerny, J., Castillo-Aja, R., Melgar, D., Lagos, M., ... & Ruiz-Fernández, A. C. (2020). Sand deposits reveal great earthquakes and tsunamis at Mexican Pacific Coast. Scientific Reports, 10(1), 1-10.

Satake, K., K. Shimazaki, Y. Tsuji, and K. Ueda, (1996) Time and size of a giant earthquake in Cascadia inferred from Japanese tsunami records of January 1700, Nature, 379, 246–249, (1996).

Satake, K., Wang, K., & Atwater, B. F. (2003) Fault slip and seismic moment of the 1700 Cascadia earthquake inferred from Japanese tsunami descriptions. Journal of Geophysical Research: Solid Earth, 108(B11), (2003)

Schmalzle, G. M., McCaffrey, R., & Creager, K. C. (2014) Central Cascadia subduction zone creep. Geochemistry, Geophysics, Geosystems, 15(4), 1515-1532, (2014).

Shennan, I., Long, A.J., Rutherford, M.M., Green, F.M., Innes, J.B., Lloyd, J.M., Zong, Y. and Walker, K.J. (1996) Tidal marsh stratigraphy, sea-level change and large earthquakes, I: a 5000 year record in Washington, USA. Quaternary Science Reviews, 15(10), pp.1023-1059.

Small, D.T., & Melgar, D., (2020) Geodetic Coupling Models as Constraints on Stochastic Earthquake Ruptures: An Example Application to PTHA in Cascadia. Earth and Space Science Open Archive, doi:10.1002/essoar.10504702.1.

Tozer, B., Sandwell, D. T., Smith, W. H., Olson, C., Beale, J. R., & Wessel, P. Global bathymetry and topography at 15 arc sec: SRTM15+. Earth and Space Science, 6(10), 1847-1864. (2019)

Walton, M. A., Staisch, L. M., Dura, T., Pearl, J. K., Sherrod, B., Gomberg, J., ... & Wirth, E. Toward an Integrative Geological and Geophysical View of Cascadia Subduction Zone Earthquakes. Annual Review of Earth and Planetary Sciences, 49.

Wang, P. L., Engelhart, S. E., Wang, K., Hawkes, A. D., Horton, B. P., Nelson, A. R., & Witter, R. C. (2013) Heterogeneous rupture in the great Cascadia earthquake of 1700 inferred from coastal subsidence estimates. Journal of Geophysical Research: Solid Earth, 118(5), 2460-2473.

Whitmore, P., Benz, H., Bolton, M., Crawford, G., Dengler, L., Fryer, G. & Oppenheime, D. (2008) NOAA/West coast and Alaska tsunami warning center Pacific Ocean response criteria. Science of Tsunami Hazards.

Williamson, A., Melgar, D., & Rim, D. The Effect of Earthquake Kinematics on Tsunami Propagation. Journal of Geophysical Research: Solid Earth, 124(11), 11639-11650. (2019).

Wirth, E. A., & Frankel, A. D. (2019). Impact of Down-Dip Rupture Limit and High-Stress Drop Subevents on Coseismic Land-Level Change during Cascadia Megathrust Earthquakes. Bulletin of the Seismological Society of America, 109(6), 2187-2197, (2019).

Witter, R.C., H.M. Kelsey, and E. Hemphill-Haley (2003) Great Cascadia earthquakes and tsunamis of the past 6700 years, Coquille River estuary, southern coastal Oregon, Geological Society of America Bulletin, v. 115, p. 1289-1306, doi: 10 .1130 /B25189 .1.

Yamaguchi, D. K., Atwater, B. F., Bunker, D. E., Benson, B. E., & Reid, M. S. (1997) Tree-ring dating the 1700 Cascadia earthquake. Nature, 389(6654), 922-923, (1997)

Ye, L., Lay, T., Kanamori, H., & Rivera, L. (2016) Rupture characteristics of major and great (Mw≥ 7.0) megathrust earthquakes from 1990 to 2015: 1. Source parameter scaling relationships. Journal of Geophysical Research: Solid Earth, 121(2), 826-844, (2016).